PALEOCEANOGRAPHY, VOL. 16, NO. 3, PAGES 317-329, JUNE 2001

Could the Late Permian deep ocean have been anoxic?

R. Zhang, M. J. Follows, J. P. Grotzinger, and J. Marshall

Department of Earth, Atmospheric, and Planetary Sciences, Massachusetts Institute of Technology, Cambridge, Massachusetts

Abstract. Models of ocean circulation and biogeochemical cycles are used to speculate about possible mechanisms of deep-sea anoxia across the Permo-Triassic boundary. Two modes of likely Late Permian ocean thermohaline circulation are identified: a vigorous "thermal mode" driven by cooling in southern polar latitudes and a weaker "haline mode" driven by evaporation from the subtropics. We find that the thermal mode, typical of climates such as our own, is unlikely to surpport deep-sea anoxia. The haline mode, which might exist in warm climates with enhanced hydrological cycles, can lead to significant but periodic depletion of oxygen in the Panthalassic deep ocean. However, owing to the inherent instability of the haline mode, a deep-sea anoxia persisting for millions of years is not clearly supported by this study, though mechanisms emerge which might be consistent with the observed record. The enhanced hydrological cycle (or reduced oceanic diapycnal mixing) required to obtain the haline mode remain unconstrained for the Late Permian.

1. Introduction

Recently, it has been suggested that a long-term deep-sea anoxic event straddled the Permo-Triassic boundary 250 million years ago. It has been proposed that anoxia reached the bottom of the Late Permian ocean, extended laterally several thousand of kilometers, and had a duration of ~ 20 million years [*Isozaki*, 1997; *Kajiwara et al.*, 1994]. The event has been linked to the End Permian mass extinctions as a potential causal mechanism [*Knoll et al.*, 1996]. Hypotheses for deep-sea anoxia include ocean stagnation [*Knoll et al.*, 1996], strong thermohaline ocean circulation driven by polar convection [*Sarmiento et al.*, 1988], and low-latitude sinking of warm, saline, oxygen-depleted surface water [*Railsback et al.*, 1990]. Each of these mechanisms has different implications for Late Permian ocean circulation and biogeochemistry. In this paper, we apply insights from box models and three-dimensional (3-D) circulation and biogeochemical models to explore conditions under which deep-sea anoxia might have developed in the Late Permian ocean.

In this study we only address the issue of deep-sea anoxia, but in so doing provide some physical and biogeochemical context for the proposed mass extinction hypotheses. Although many aspects of the sedimentary, paleontological, and geochemical record are consistent with Late Permian ocean anoxia at shallower depths [*Erwin*, 1994; *Wignall and Twitchett*, 1996], our goal here is to evaluate claims [*Isozaki*, 1997; *Kajiwara et al.*, 1994] that the deep ocean (depths > 3000 m) could have become anoxic and sustained this condition more or less continuously for tens of millions of years. This is important given that the records of Late Permian deep-sea anoxia are retained within obducted accretionary complexes [*Isozaki*, 1997; *Kajiwara et al.*, 1994] and that such rocks are not necessarily representative of the sea bottom formed in the open ocean [*Saleeby*, 1992; *Ishiwatari*, 1991]. Instead, subduction complexes and obducted blocks of oceanic crust could be interpreted to represent closure of back arc basins rather than open ocean basins. Thus it is possible that the geochemical records are from a restricted part of the Late Permian ocean, similar to the modern Cariaco basin [*Zhang and Millero*, 1993], rather than indicative of the great expanse of the Panthalassic deep ocean. At this time, only two data points in Japan and western Canada are available for supporting Late Permian deep-ocean anoxia. Until new data become available, the only means to further test the notion of Panthalassic deep-ocean anoxia is through theoretical and numerical simulation of ocean circulation and biogeochemical patterns. In this manner, physically implausible scenarios can be eliminated, providing a clearer image of what processes would have been required to induce an anoxic state which could have persisted or recurred for millions of years.

In section 2 we develop and study a box model of the phosphorous and oxygen cycle and study its properties and implications for deep-sea anoxia. We go on to embed the biogeochemical model in a 3-D ocean circulation model and apply it to successfully reproduce the gross oxygen and phosphorous distribution in the modern ocean circulation. In section 3 we apply the same model to the Late Permian ocean and study its circulation and anoxia scenarios. Summary and conclusions are presented in section 4.

Paper number 2000PA000522.
0883-8305/01/2000PA000522$12.00

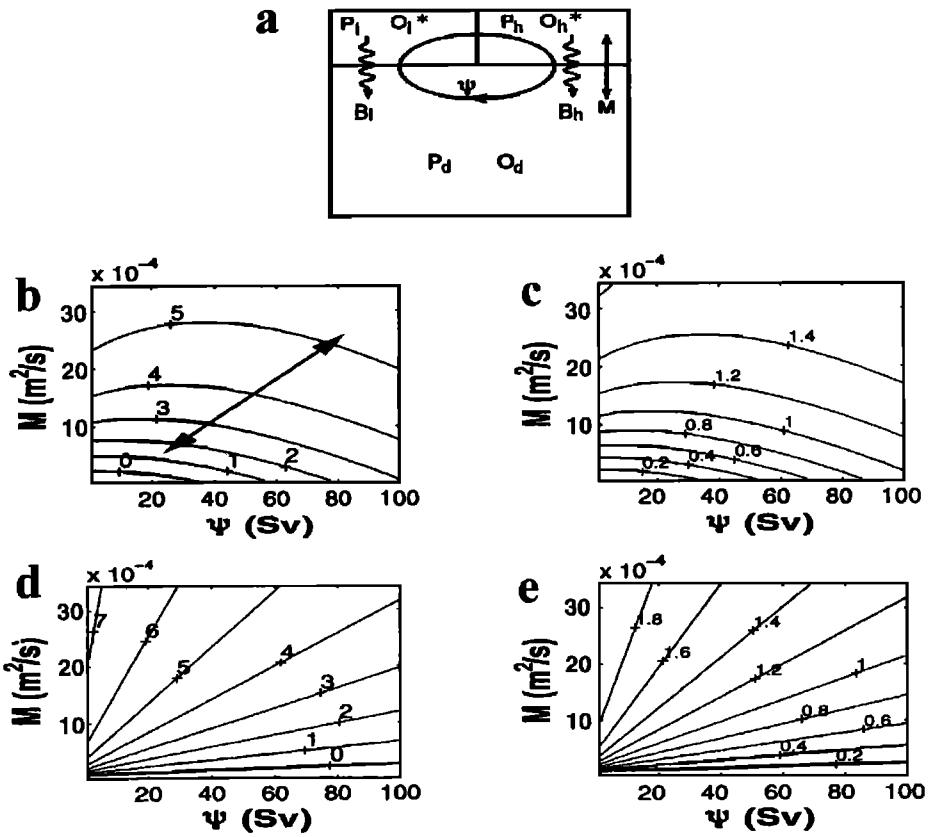

Figure 1. Box model of the phosphorous and oxygen cycle in the ocean. (a) Schematic diagram of the three-box model: the two top boxes are used to represent the euphotic zone of low latitudes and high latitudes, and the third box represents the abyssal ocean beneath. P_l, P_h, and P_d are the phosphorous concentrations in each box. O_l^* and O_h^* are the surface equilibrium oxygen concentration with respect to local atmospheric partial pressure of oxygen and the temperature- and salinity- dependent solubility [*Weiss*, 1970]. O_d is the oxygen concentration of the abyss. B_l and B_h are the organic matter export rates from boxes of the euphotic zone respectively. ψ is the thermohaline transport rate, and M is the rate of mixing between the high latitude surface and deep ocean due to deep convective mixing. (b) O_d (mL/L) and (c) P_h (μmol/kg) in the (M/ψ) plane for parameter ranges encompassing those of the modern ocean. The oxygen concentration generally decreases if thermohaline circulation rate and/or convective mixing rate decreases. Mixing and overturning rates are not independent, indicated here by the sloping schematic trajectory. (d) O_d (mL/L) and (e) P_h (μmol/kg) in the (M/ψ) plane for the limit case $\lambda_l \to \infty$ and $P_h \gg P_c$.

2. Simplified Biogeochemical Model

2.1. Three-Box Model of Phosphorous and Oxygen Cycle

We employ a simple three-box model of ocean phosphorous and oxygen cycling to examine the interplay of circulation and biogeochemistry and seek to understand the criteria under which deep oceanic anoxia may be possible.

The model is depicted schematically in Figure 1a, with two boxes representing the low- and high-latitude euphotic zone and a third box representing the deep ocean. Tracers are advected by the meridional overturning circulation ψ and experience deep, convective mixing at high latitudes, parameterized by mixing coefficient M. The model somewhat resembles previous studies [e.g., *Sarmiento et al.*, 1988] but with some significant differences. One important aspect of the box model is that the particulate export of phosphorous is parameterized with the same nutrient- and light-limiting function as used in the three-dimensional experiments discussed in section 2.2.

We assume that the global ocean phosphorus burden is constant and, assuming volume and nutrient conservation for each box, derive governing equations for phosphorus in the surface boxes, determined by advection, convective mixing, and the particulate export of organic matter:

$$V_l \frac{dP_l}{dt} = \psi P_d - \psi P_l - V_l B_l, \tag{1}$$

$$V_h \frac{dP_h}{dt} = \psi P_l - \psi P_h + \frac{A_h M}{h}(P_d - P_h) - V_h B_h. \tag{2}$$

Here V_l, V_h, and V_d are the volumes of the boxes of the low-latitude euphotic zone, high-latitude euphotic zone, and deep ocean, A_h is the surface area of the high-latitude surface box,

h is the convective mixing depth in the high latitude region, and t is the time.

The sinking particulate export of nutrients B is limited by light and nutrients thus:

$$B = \frac{\Phi\epsilon}{h_e}\frac{P}{P+P_c}. \quad (3)$$

Here P is the total phosphorous concentration of the surface euphotic zone. $\Phi\epsilon/h_e$ is the vertical divergence of the flux of short wave solar radiation Φ in the euphotic layer, thickness h_e, scaled by the "light utilization efficiency" ϵ [*Parsons*, 1988]. Light limitation is enforced by assuming the flux divergence of short wave solar radiation provides an extreme upper bound on the rate of new and export production (i.e., the rate of new and export production may not exceed that of primary production). Nutrient limitation of export is enforced by $P/(P+P_c)$. Here P_c is the nutrient concentration at which particulate export becomes light limited (not to be confused with a half saturation coefficient for primary production). Hence

$$P_c = \frac{\Phi\epsilon}{h_e\lambda}, \quad (4)$$

where λ is a global rate constant which characterizes the ocean-wide efficiency of biological flushing of nutrients from the euphotic zone. Here $1/\lambda$ represents the typical residence time of a phosphorus atom in the euphotic zone with respect to export on a biogenic particle. When $P \ll P_c$, particulate export is proportional to the local phosphorous concentration, ensuring nutrient limitation at low phosphorous concentrations. When $P \gg P_c$, export is proportional to the incident flux of short wave solar radiation $\Phi(y,t)$, a function of latitude and season. We use this parameterization of particulate export of nutrients both in the box model and in the three-dimensional model experiments discussed in section 2.2. For the box model, in the high-latitude surface box, $B_h = \lambda_h P_h P_c/(P_h+P_c)$. For the low-latitude surface box we assume that light is never limiting, and hence $B_l = \lambda_l P_l$. A statement of conservation of total ocean phosphorus, in conjunction with (1) and (2), completes the description of the box model phosphorus cycle.

In general, surface oxygen concentrations are observed to be close to local equilibrium with respect to the atmosphere owing to the rapid air-sea equilibration timescales for the mixed layer [*Wanninkof*, 1992]. Hence, in this box model we make the simplifying assumption that the surface oxygen concentrations are set to the equilibrium values, $O_l = O_l^*$ and $O_h = O_h^*$, as determined from local temperature, salinity, and atmospheric partial pressure of O_2 [*Weiss*, 1970]. Oxygen concentration in the deep-ocean box O_d is determined by advection, high-latitude mixing, and remineralization of particles below the euphotic zone:

$$V_d\frac{dO_d}{dt} = \psi O_h^* - \psi O_d - \frac{A_h M}{h}(O_d - O_h^*) + R(V_l B_l + V_h B_h). \quad (5)$$

Oxygen is consumed during remineralization below the euphotic zone according to the Redfield stoichiometry, where R is Redfield ratio of $O:P$ [*Takahashi et al.*, 1985].

Solving (1)–(5) for steady state ($d/dt = 0$) reveals

$$O_d = O_h^* + RP_0 f^*(\psi, M, P_0), \quad (6)$$

where $f^*(\psi, M, P_0) = 1 - P_h/P_0$. Here

$$P_h = \frac{1}{2(\frac{A_h M}{h}+\psi)}\{S + [S^2 + 4P_c P_0(\frac{A_h M}{h} + \frac{\psi^2}{\psi+\lambda_l V_l})(\frac{A_h M}{h}+\psi)]^{\frac{1}{2}}\}, \quad (7)$$

$$S = P_0(\frac{A_h M}{h} + \frac{\psi^2}{\psi+\lambda_l V_l}) - (1 + \lambda_h V_h + \frac{A_h M}{h})P_c. \quad (8)$$

Here $f^*(\psi, M, P_0)$ is a function of the ocean transport characteristics (ψ, M) and the global mean concentration of phosphorus in the ocean P_0. The deep-ocean oxygen is set through ventilation by oxygen-rich waters from the high-latitude surface (first term on right of (6)) and reduced by remineralization of the flux of biogenic particles (second term on right of (6)).

The dependence of deep-ocean oxygen concentration and high-latitude surface phosphorous concentration on ocean transport parameters, for this model, is shown in Figure 1. Several notable inferences can be drawn: (1) increasing thermohaline overturning rate increases oxygenation of the deep waters in most parameter ranges (Figure 1b, variable values for the modern ocean are listed in Table 1), (2) increased phosphorous loading of the ocean reduces deep-ocean oxygen concentrations, and (3), decreased equilibrium oxygen concentration of sinking surface waters leads to decreased deep-ocean oxygen concentrations.

Here a criterion of 1 mL/L is chosen below which we assert that the deep-ocean oxygen is significantly depleted in dissolved oxygen (not necessarily anoxic) relative to the modern deep ocean, which typically has $\sim$ 4mL/L of dissolved oxygen. The box model result is qualitatively different from that of *Sarmiento et al.* [1988], who found that increasing thermohaline overturning rate decreased oxygenation of the deep ocean in a somewhat similar box model. (The value of M in our model can be directly compared with the value of F_{hd} of *Sarmiento et al.* [1988] using the linear relation: $F_{hd} = A_h M/h$). How can we reconcile the different result? *Sarmiento et al.* [1988] chose to specify the organic particle flux in the downwelling branch and assumed that surface nutrients in the upwelling branch are completely utilized and instantly exported as particles. This represents a limit case of the model described above, where $\lambda_l \to \infty$ and $P_h \gg P_c$. In this limit the solution of our model for P_h is

$$P_h = \frac{P_0\frac{A_h M}{h} - \lambda_h V_h P_c}{\frac{A_h M}{h} + \psi}. \quad (9)$$

Table 1. Box Model Variable Values for the Modern Ocean

Variable	Value
A_h (High latitude surface area)	8.75×10^{13} m^2
h_e (Euphotic layer depth)	100 m
h (Convective mixing depth)	2000 m
V_l (Low latitude euphotic zone volume)	8.75×10^{15} m^3
V_h (High latitude euphotic zone volume)	8.75×10^{15} m^3
λ_l (Low latitude organic matter export rate)	1/(30 months)
λ_h (High latitude organic matter export rate)	1/(30 months)
P_0 (Mean ocean phosphorus concentration)	2.07 μmol/kg
P_c (Light-limited phosphorus concentration)	0.9 μmol/kg
R (Redfield ratio of O:P)	-175
O_h^* (High latitude surface equilibrium oxygen concentration)	7.5 mL/L

This is indeed consistent with equation (8) of *Sarmiento et al.* [1988]. For comparison, we illustrate this case in Figure 1d, which shows similar trends to Figure 4 of *Sarmiento et al.* [1988], where $\partial O_d/\partial\psi < 0$ over all of M, ψ space. Stronger thermohaline overturning supplies more nutrients to the surface in the upwelling branch and stronger particle export, so leading to deep-sea oxygen depletion. However, this limit represents a very special case. More generally, we find $\partial O_d/\partial\psi > 0$ over much of M, ψ space.

We have chosen to use the same nutrient- and light-limited parameterization of export production in this box model as is used in the three-dimensional experiments in section 2.2. The three-dimensional experiments demand such a representation to allow the biogeochemistry to respond appropriately when the ocean bathymetry and climate are significantly modified, and we cannot usefully impose particle flux distributions in the three-dimensional experiments. We recognize, however, the simplicity of our parameterization which omits other, possibly important, limiting nutrients. We will demonstrate that our export parameterization reproduces the broad features of the modern ocean oxygen distribution in a three-dimensional model (section 2.2) and that the box model using this scheme successfully predicts the sensitivity of deep ocean oxygen in the 3-D model to changes in thermohaline overturning (section 3.2). Inferences from the box model are now used to guide and are tested by a 3-D ocean circulation and biogeochemistry model which also yields insights into the processes that control the detailed vertical and horizontal distribution of oxygen.

2.2. Three-Dimensional Biogeochemical Model

The 3-D biogeochemical model is based on the same parameterizations of nutrient and oxygen cycling as the box model but with ocean circulation fields u, v, w (zonal, meridional, vertical velocity), T (temperature), and S (salinity) and convective index, used to drive the biogeochemical model taken from an ocean model developed by *Marshall et al.* [1997a, 1997b]. The physical model, which uses height as a vertical coordinate, is configured at a resolution of $2.8^o \times 2.8^o$ in the horizontal and 15 levels in vertical in a domain of irregular geometry to represent the complexities of the ocean basins. We use "no-slip" conditions at the lateral walls and bottom and insulating thermal boundary conditions. The horizontal and vertical viscosity are 5×10^5 and 10^{-3} m^2/s, respectively, and the horizontal and vertical diffusion coefficients are 10^3 and 5×10^{-5} m^2/s, respectively, in close accord with *Bryan* [1986]. Tracers are advected with the "transformed eulerian mean" velocity [*Gent and McWilliams*, 1990], and convection is parameterized as described in section 5 of *Marshall and Schott* [1999]. The resulting model, when forced by observed modern-day winds and air-sea fluxes, yields a plausible representation of the coarse-grained circulation of the modern ocean, with a global overturning circulation of strength 20 Sv and a northward meridional heat transport peaking at 1.5 PW (petawatts).

The equation for phosphorous concentration P in every grid cell is

$$\frac{\partial P}{\partial t} + \nabla\bullet(\mathbf{U}P) = \nabla\bullet(\kappa\nabla P) + M + B. \qquad (10)$$

Here M represents convective mixing, $\mathbf{U}$ is monthly averaged eulerian mean velocity fields (u, v, w), $\nabla\bullet(\kappa\nabla P)$ is the parameterized subgrid-scale tracer mixing, and B is the net organic matter export flux from the base of each grid cell given by (3) and (4) within the euphotic zone. Below the euphotic zone we have

$$B = -\frac{\partial F(z)}{\partial z} \qquad z < -h_e, \qquad (11)$$

$$F(z) = F(-h_e)\exp[(h_e + z)/z^*], \qquad (12)$$

$$F(-h_e) = -\int_{-h_e}^{0} \frac{\Phi\epsilon}{h_e}\frac{P}{(P + P_c)}dz. \qquad (13)$$

The sinking particle flux is modeled by a specified profile which decays exponentially [*Najjar et al.*, 1992] with depth.

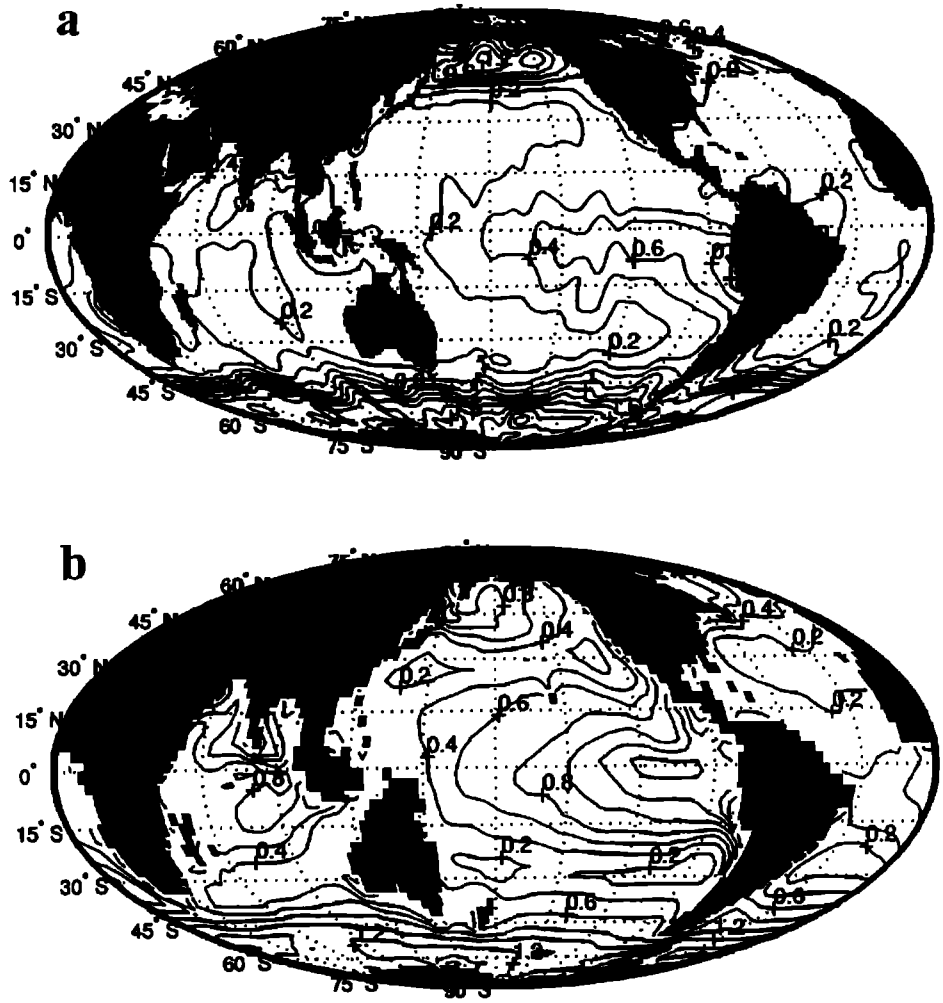

Figure 2. Surface nutrient concentration of modern ocean. (a) Surface phosphorous concentration of the modern ocean (μmol/kg) according to the Levitus94 [*Levitus et al.*, 1994] observational data. (b) Surface phosphorous concentration obtained from the three-dimensional (3-D) biogeochemical model driven by an ocean circulation model.

Here h_e is the depth of the euphotic zone, taken to be the top two layers (120 m) in the model. Z^* is the scale height for remineralization and is chosen to be 400 m, broadly consistent with the sediment trap observations of *Lohrenz et al.* [1992] in the Sargasso Sea. $P_c = \Phi\epsilon\,/(h_e\lambda)$ is just as defined in the three-box model (equation (4)), ϵ is the average light utilization efficiency with a value of 3.5×10^{-5} μmol P per joule of incident short wave solar radiation [*Parsons et al.*, 1988], and Φ is the net flux of incident short wave solar radiation as a function of latitude, season [*Paltridge and Platt*, 1976], and depth [*Parsons et al.*, 1988], specifying an albedo which varies with latitude and season [*North et al.*, 1981]. Here λ is a global export coefficient, as defined in the three-box model; we find a value of $\lambda = 1/(30$ months) gives reasonable P distribution, and it is an appropriate export timescale over much of the (high nutrient, low chlorophyll) ocean. Below the euphotic zone, sinking organic matter from the base of the upper layer is assumed to be remineralized instantly, while within the euphotic zone, no remineralization is allowed. Sedimentary processes and river runoff are not represented, and so the ocean burden of phosphorous is conserved.

The prognostic equation for oxygen concentration O_2 in each grid cell has the following form:

$$\frac{\partial O_2}{\partial t} + \nabla\bullet(UO_2) = \nabla\bullet(\kappa\nabla O_2) + M + R\,B + \frac{V_p(O_2^* - O_2)}{\Delta z(k=1)}\delta(k{=}1). \qquad (14)$$

The air-sea flux of oxygen F_{O_2} is parameterized employing a piston velocity V_p [*Wanninkof*, 1992]; thus $F_{O_2} = -V_p(O_2 - O_2^*)$, where O_2^* is the surface equilibrium dissolved oxygen concentration. Here $\delta(k=1)$ is a delta function, and k labels vertical layers, so the term $V_p(O_2^* - O_2)$ is only active in the surface layer of the model.

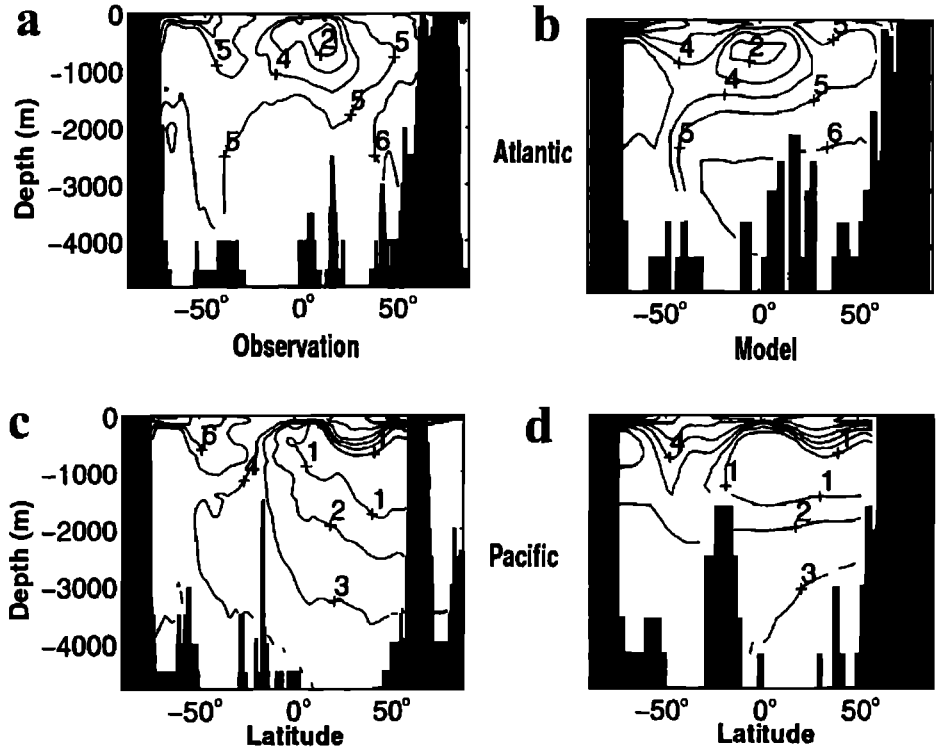

Figure 3. Vertical sections of oxygen through the modern ocean (mL/L) according to (left) the Levitus94 [*Levitus and Boyer*, 1994] observational data compared with (right) those obtained from the 3-D biogeochemical model driven by an ocean circulation model. (a and b) Atlantic (along 22.5°W) and (c and d) Pacific (along 143.5°W)

The resulting three-dimensional biogeochemical model is spun up from a uniform distribution of phosphorous (2.07 μmol/kg) (unless otherwise stated) and oxygen (6.7 mL/L) until an equilibrium state is reached. Pleasingly, when driven (offline) by the simulated modern ocean circulation pattern, the biogeochemical model yields distributions of phosphorous (Figure 2) and oxygen (Figure 3) that are broadly consistent with observations of the modern ocean. For example, Figure 3 shows the signature of reduced oxygen (high nutrient) concentrations in Antarctic Intermediate Water of the Atlantic. High productivity in the tropics induces consumption of oxygen below, forming a local subsurface minimum of oxygen. Sinking of North Atlantic Deep Water in the North Atlantic oxygenates the deep ocean, a signature clearly visible into the Southern Hemisphere. The older waters of the deep Pacific are relatively depleted in oxygen owing to cumulative remineralization of sinking organic matter. Productivity in North Pacific surface waters results in the development of anoxia at intermediate levels, the only example of widespread anoxia in the modern ocean. However, the abyss of the modern ocean is rich in oxygen ($\sim$ 4 mL/L) because, consistent with our box model, there is active polar sinking and convective mixing.

Since the biogeochemical model does not directly depend on modern observations but can successfully reproduce them, we now use the same model to guide speculations about cycles in the Late Permian. However, what was the pattern of ocean circulation in the Late Permian? That depends on the prevailing meteorology and the distribution of land and sea in the Late Permian.

3. Application to Late Permian

3.1. Physical Modeling of the Late Permian

The Late Permian land-sea distribution was quite different from that of today. The supercontinent Pangaea extended from the North Pole to the South Pole, and the Panthalassic superocean covered nearly 70% of the Earth's surface and connected to the small, narrow Tethys sea. A paleobathymetry was obtained from D. B. Rowley and used to configure our ocean circulation model for the late Permian (Figure 4a). Although epicontinental regions are represented by variable depths between 0 and 4000 m in the reconstruction, the deep ocean is assumed to have a flat bottom with a uniform depth of 4000 m due to lack of other evidence. The ocean domain of the model extends from 70°N to 70°S. The prevailing meteorological conditions are even less certain, and so we chose two scenarios. Scenario 1, based on an atmospheric circulation model of the Late Permian [*Kutzbach et al.*, 1990; *Kutzbach and Gallimore, 1989*], corresponds to a warm climate with enhanced greenhouse effect ($5\times CO_2$) and reduced solar luminosity (1% decrease). It gives (rel-

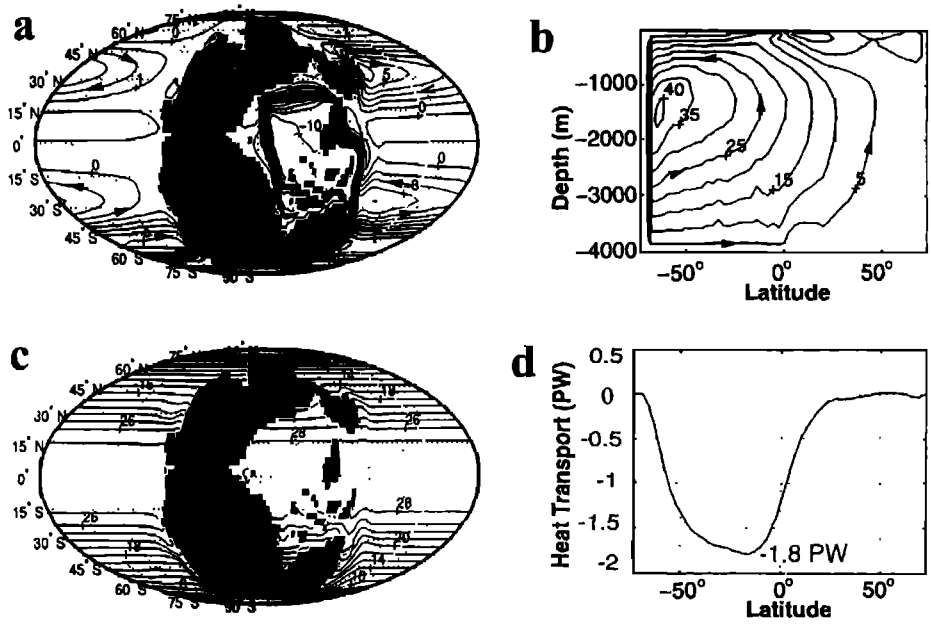

Figure 4. Possible thermal mode Late Permian ocean circulation. (a) Horizontal stream function (in Sv) of the Late Permian "thermal mode", revealing a superposition of the wind-driven circulation (Sverdrupian gyres) and the thermohaline circulation looping through the Tethys Sea. (b) Overturning stream function (in Sv) of the Late Permian thermal mode. (c) Sea surface temperature (SST, °C). (d) Meridional ocean heat transport (PW).

ative to the modern) a weak surface wind stress τ (Figure 5a), a weak pole-equator surface temperature gradient (Figure 5b), and a freshwater flux $E - P$, which reached a maximum of 0.4 m/yr (Figure 5c), compared to a modern value of $\sim$ 0.6 m/yr. Scenario 2 prescribes the modern surface wind stress and surface temperature but the same $E - P$ pattern as in scenario 1. Scenario 2 provides a strong surface wind stress(Figure 5d) and a strong pole-equator surface temperature gradient (Figure 5e) in contrast to scenario 1. All surface forcing patterns were zonally averaged, and adjusted to be symmetric about the equator, and then these zonally-averaged fields were used to drive the 3-D circulation. Mixed surface boundary conditions were employed: the sea surface temperature (SST) is relaxed to a prescribed surface temperature [*Haney*, 1971], but to avoid spurious feedbacks between the freshwater flux and local salinity, the effect of precipitation is represented as a salinity flux, thus $Q_S = S_o(E - P)$, where S_o is the mean surface salinity of the ocean. The mean salinity of the ocean assumed is 34.6 practical salinity units (psu).

3.1.1. Thermal mode ocean circulation. The ocean circulation resulting from scenario 1 is highly asymmetric (Figure 4), with strong sinking in the southern high latitudes reaching a maximum of 40 Sv (Figure 4b), considerably stronger than the modern. Large southward heat fluxes ($\sim$1.8 PW, Figure 4d) result in the South Pole being some 6°C warmer than the North Pole (Figure 4c). Vigorous deep-reaching convection occurs in the southeast corner of the superocean, adjacent to western South America and western Antarctica, maintaining the deep water at $\sim$ 5°C there. We find that this thermally driven circulation is rather stable. If the model is driven as in scenario 2, we still find an equilibrium solution with sinking in southern high latitudes. If the circulation is perturbed for many hundreds of years to induce Northern Hemispheric sinking by, for example, adding a net evaporation (0.1 m/yr) in the northern high latitude and a net precipitation (0.1 m/yr) in the southern high latitude, the solution always switches back to sinking in southern high latitude when symmetric forcing is restored [see also *Marotzke and Willebrand*, 1991]. This polar overturning circulation is driven primarily by air-sea heat flux (a thermal mode).

This model result differs from the symmetric ocean circulation pattern for idealized ocean at Pangaean time obtained by *Kutzbach et al.* [1990] and must be a consequence of the different land-sea distribution and different surface boundary conditions. Evidently, asymmetries in the Late Permian land-sea distribution predisposes modeled deepwater formation in the south in our experiments, and we do not restore the surface salinity to prescribed symmetric values. It is interesting to note that a Late Permian southern high latitude fossil forest deposit indicates warm polar climates [*Taylor et al.*, 1992], consistent with a strong southward ocean heat transport associated with sinking in southern high latitudes.

3.1.2. Haline mode ocean circulation. Previous modeling studies have suggested that the thermohaline circulation is a nonlinear system supporting multiple solutions which are highly sensitive to the surface freshwater forcing [*Stommel*, 1961; *Bryan*, 1986; *Manabe and Stouffer*, 1988;

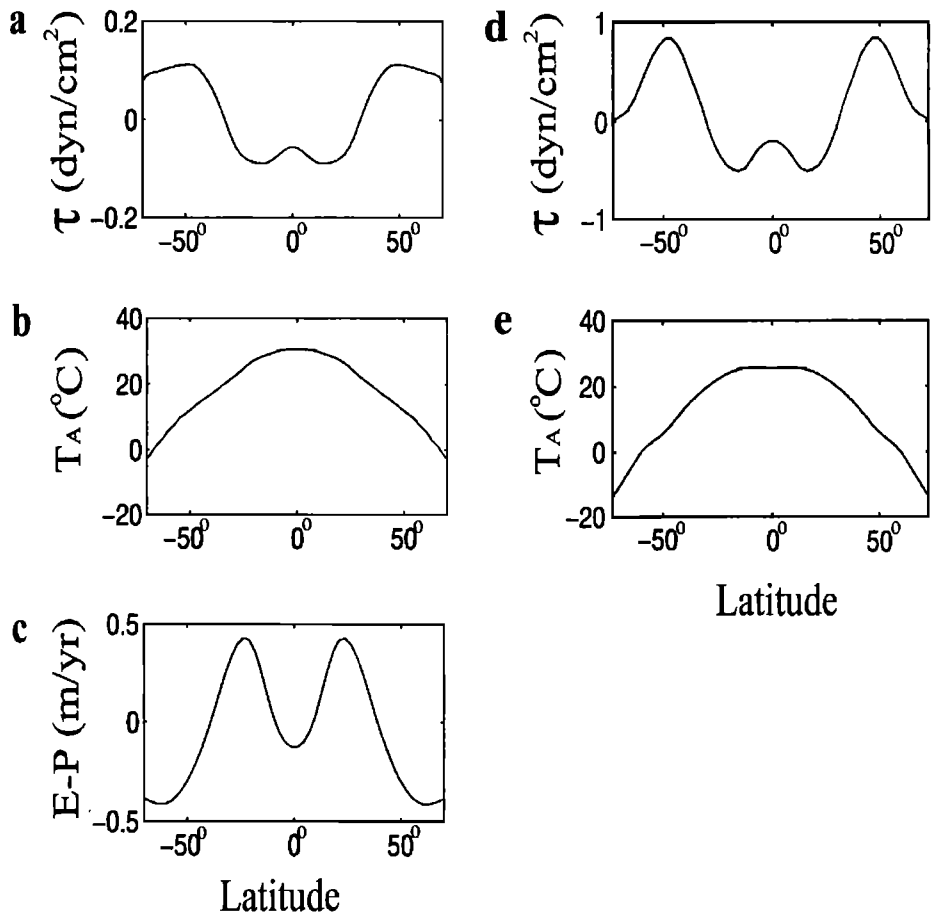

Figure 5. Surface forcing scenario 1 (Figures 5a-5c) and surface forcing scenario 2 (Figures 5d and 5e). (a) Zonally averaged surface wind stress (dyn/cm^2). (b) Zonally averaged prescribed surface temperature T_A (°C). (c) Zonally averaged freshwater flux $(E-P)$(m/yr). (d) Zonally averaged surface wind stress (dyn/cm^2). (e) Zonally averaged prescribed surface temperature T_A (°C).

Marotzke and Willebrand, 1991]. We find that if the amplitude of the freshwater flux is increased relative to the heat flux beyond a certain threshold, it is possible to find a prevalent haline mode of ocean circulation in which sinking occurs in the subtropics. This has very different implications for the oxygen cycle. As discussed by *Zhang et al.* [1999], the critical amplitude of freshwater flux, beyond which the haline mode dominates, is sensitive to the diapycnal diffusivity K_z in the ocean because K_z controls the strength of the overturning circulation, meridional ocean heat transport, and hence SST and air-sea heat flux. For the values of vertical mixing assumed in our simulation of the modern circulation and the Late Permian thermal mode (discussed above in section 3.1.1) $K_z = 5 \times 10^{-5}$ m^2/s , we find that the threshold is close to 5 $(E-P)$; that is, the intensity of the hydrological cycle would have to be increased fivefold for the haline mode to dominate. Because of fundamental constraints encapsulated in the Clausius-Clapeyron relationship it is unrealistic to suppose that the Late Permian climate had such an enhanced hydrological cycle. However, the critical amplitude of freshwater flux decreases with K_z [*Zhang et al.*, 1999]. The physics that control the level of diapycnal mixing in the ocean remain uncertain even for the modern ocean and may have been different in the past. Measurements of the vertical spread of deliberate tracer releases in the main thermocline [*Ledwell et al.*, 1993] yield $K_z = 1.1 \times 10^{-5}$ m^2/s, in the lower range of that which is assumed in large-scale ocean circulation models. K_z is known to be spatially inhomogeneous, becoming larger near boundaries where tidally induced mixing processes may dominate [*Toole et al.*, 1994; *Marotzke*, 1997; *Munk and Wunsch*, 1998]. If we reduce K_z to 3×10^{-5} m^2/s, it is possible to obtain a haline mode forced with a more reasonable $(E-P)$ flux.

We set up the Late Permian ocean circulation model now with $K_z = 3 \times 10^{-5}$ m^2/s under forcing scenario 1, with 3.3 $(E-P)$ (1.3 m/yr at maximum, about twice that of the modern freshwater intensity) and found a quasi-steady solution with haline-induced sinking in the subtropics (Figure 6). In the haline mode the overturning strength is much weaker than the thermal mode ($\sim$ 14 Sv, Figure 6b) with warm and

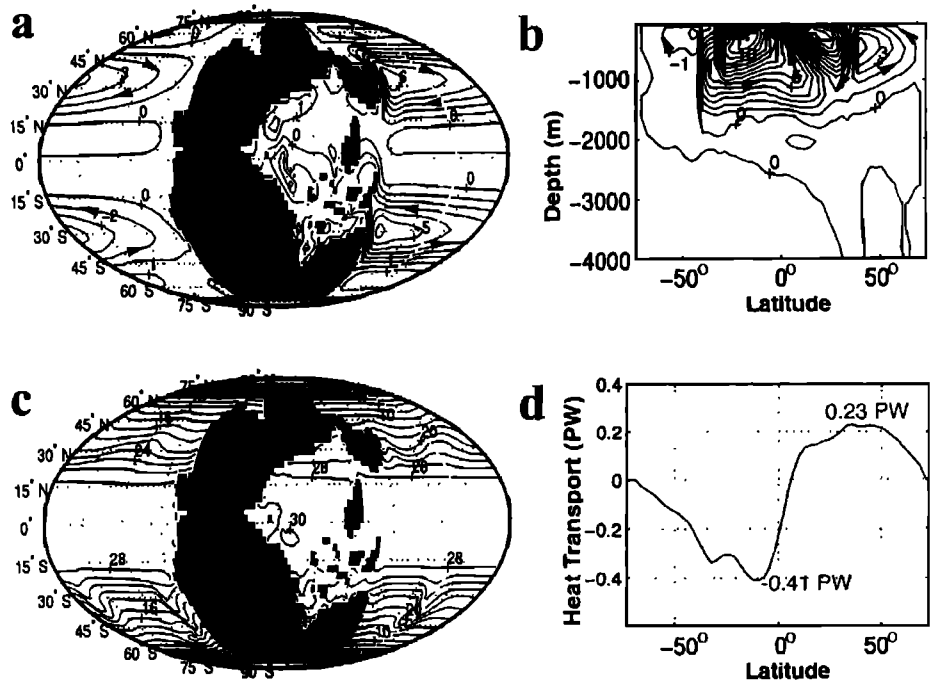

Figure 6. Possible haline mode Late Permian ocean circulation. (a) Horizontal stream function (in Sv) of the Late Permian haline mode. (b) Overturning stream function (in Sv) of the Late Permian haline mode. (c) Sea surface temperature (°C). (d) Meridional ocean heat transport (PW).

salty intermediate water formed in the subtropics induced by net evaporation. Less heat is transported poleward (Figure 6d), and the SST in both polar regions is $\sim 0°C$ (Figure 6c). The deep ocean becomes stagnant and well stratified. It is significant that unlike the thermal mode, the haline mode is prone to instability [*Marotzke*, 1989]. In the haline mode the surface waters in polar regions are cold and fresh while the deep waters below are warm and salty. If a small perturbation mixes deep salty water up from below, cooling at the surface can induce polar convection, switching the ocean to the thermal mode. Once the energy is discharged, the ocean can gradually return to the haline mode, if $E - P$ forcing continues to dominate. An oscillation is thus possible between thermal and haline mode [*Huang*, 1994]. The time scale of the oscillation is of the order of hundred or thousand of years and depends on the amplitude of $E - P$ and K_z. In this particular case the timescale of the oscillation is ~ 3330 years.

3.2. Biogeochemical Modeling of the Late Permian

3.2.1. Oxygen distribution with thermal mode ocean circulation. To explore the dissolved oxygen distribution implied by the Late Permian thermal mode, we used it to drive our 3-D biogeochemical model to equilibrium. We started from the same uniform distribution of phosphorous and oxygen and a surface oxygen concentration of $PO_2 \sim 0.21$ bars, as in the modern. Although at intermediate levels, anoxic regions exist (Figure 7a), the oxygen concentration in the deep ocean is everywhere high, ~ 4.7 mL/L, especially below the deepwater-forming region in the southern high latitudes, where the deep-ocean oxygen concentration is ~ 5 mL/L (Figure 7b). Doubling the mean ocean phosphorous concentration P_0 in the 3-D model lowers oxygen concentrations, consistent with intuition gained from the box model, but we still find the minimum deep ocean oxygen concentration of ~ 3.6 mL/L. The 3-D model is less sensitive to P_0 than the box model owing to its higher vertical resolution; the intermediate level where the oxygen concentration is often very low is not explicitly represented in the three-box model. In the general circulation model (GCM), increasing P_0 will make the intermediate low-oxygen region expand because most organic matter remineralized there, but the deepwater oxygen is not very sensitive to this aspect. In the box model the deep box gives the average oxygen concentration from intermediate level to deep ocean and is more sensitive to P_0. If the surface equilibrium oxygen concentration is reduced to $PO_2 \sim 0.14$ bars (perhaps more typical of the Late Permian [*Berner and Canfield*, 1989]), the minimum deep ocean oxygen concentration is lowered to ~ 2.7 mL/L. Even when a power law profile of sinking organic matter flux is used [*Martin et al.*, 1987], in which more organic matter sinks into the deep ocean consuming oxygen, the minimum deep ocean oxygen concentration is ~ 3.2 mL/L. As expected from our simple box model, it is very difficult to obtain deep-sea anoxia with the vigorous overturning circulation typical of the presumed Late Permian thermal mode.

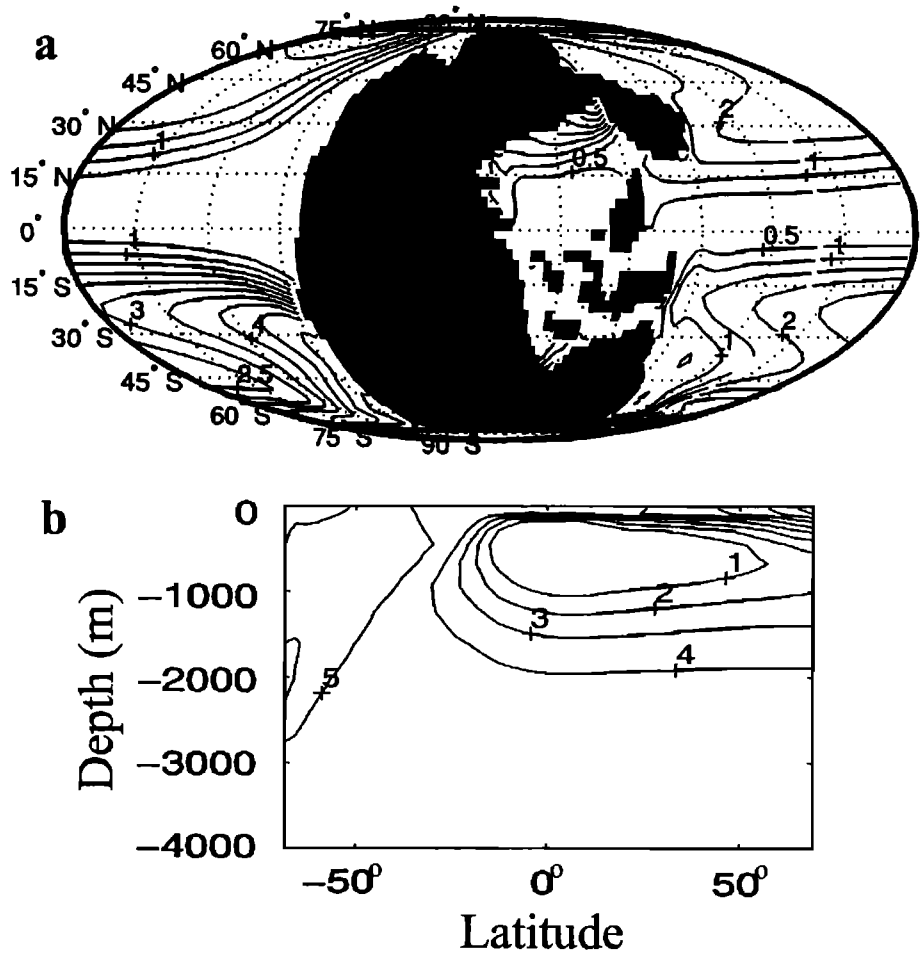

Figure 7. Possible oxygen distribution with the Late Permian thermal mode ocean circulation. (a) Oxygen distribution (mL/L) at horizontal section at depth z=500 m. (b) Oxygen distribution (mL/L) at vertical section along 130°E.

Before going on, we note that in a recent study, *Hotinski et al.* [2001] also performed model studies relating to deep-sea anoxia in the Late Permian. In their study, a circulation model forced with a reduced meridional temperature gradient led to a weakened thermal mode circulation and widespread anoxia in the model's deep ocean. This is consistent with the trends suggested by our box model in that a reduction of thermohaline overturning leads to lower deep-sea oxygen concentrations. In contrast to the experiments presented here, *Hotinski et al.* [2001] find a widespread, deep-sea anoxia in a Permian ocean with a thermal mode circulation. The difference probably lies in the details of their biogeochemical model in which negative oxygen concentrations are allowed when oxidation of organic matter occurs in the absence of dissolved oxygen. Strongly negative oxygen concentrations from intermediate depths may be diffused down into the abyss leading to apparent anoxic conditions. We prefer not to allow negative oxygen concentrations in the 3-D biogeochemical model presented here.

3.2.2. Oxygen distribution with haline mode ocean circulation. When our offline biogeochemical model is driven using the Late Permian haline mode assuming modern atmospheric PO_2, we find that the mean oxygen concentration in the deep ocean is much lower than that which accompanies the thermal mode (Figure 8), and vast areas of the eastern Panthalassic deep ocean become very depleted in oxygen (Figure 9). This result is obtained after many thousand of years of integration, spun up from the equilibrium oxygen distribution we obtained with the thermal mode circulation. Again, this is broadly consistent with the predictions of our box model.

In this model experiment, the haline mode is sustained for ~ 2830 years between thermal mode "flushing" events. The offline biogeochemical model driven by the haline mode circulation exhibits highly depleted deep ocean oxygen as it approaches steady state, but the timescale to achieve this may be many thousands of years, in part due to the extremely sluggish ocean circulation. For a superanoxia event to persist in the geologic record the timescale for oxygen depletion must be considerably shorter than the repeat time of the thermal mode flushing events. We note here that the oxygen depletion timescale is very sensitive to the form of the

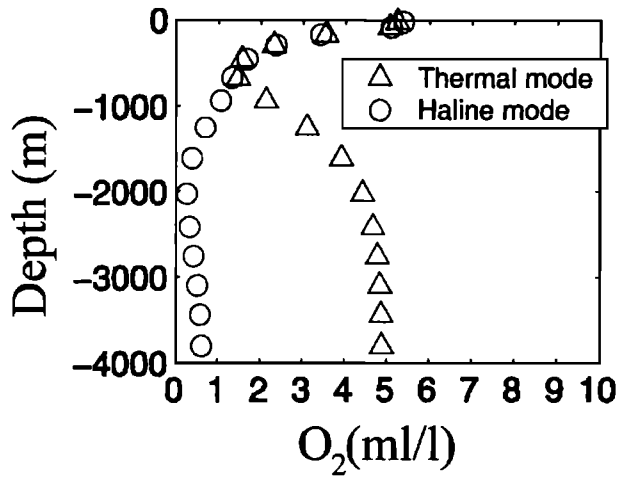

Figure 8. Vertical distribution of the horizontally averaged oxygen concentration (mL/L) for the Late Permian thermal mode and haline mode experiments, respectively, with modern ocean phosphorous burden and atmospheric PO_2 . The deep ocean of the haline mode experiment exhibits widespread, low oxygen concentrations.

particle remineralization profile. Using an exponential flux profile [*Najjar et al.*, 1992], we find a much longer oxygen depletion time (> 10,000 years) than with a power law flux profile [*Martin et al.*, 1987] (within 1000 years) though the final state is similar in both cases. The mechanism and nature of particle remineralization is currently very poorly understood. In the event that the deoxygenation timescale is shorter than the repeat time of thermal mode flushing events, sustained periods of deep-sea anoxic conditions are possible.

4. Summary

In summary, we have found that depending on the vigor of the hydrological cycle and the level of diapycnal mixing in the ocean, the late Permian ocean circulation could have been in a thermal mode or haline mode or switching one from the other, with differing implications for deep-sea anoxia. In the thermal mode, sinking in high-latitudes drives a vigorous overturning circulation with deep-reaching convection: it is inherently stable. It is very difficult for us to conceive of widespread, persistent deep-sea anoxia in the presence of such a circulation pattern, although there could have been anoxic regions at intermediate levels beneath upwelling areas, as in the Pacific and Arabian Sea today. In the haline mode, however, with warm salty intermediate water formed in the subtropics over a deep stratified ocean, the overturning circulation is much weaker and less stable than the thermal mode. This haline mode, which can be induced by an enhanced hydrological cycle and/or weak diapycnal mixing in the ocean, could support deep-sea anoxia over broad areas. Owing to the inherent instability of the haline mode it seems unlikely for the deep-sea anoxia induced by the haline mode circulation to persist uninterrupted for millions of years.

Several important issues of details remain for further investigation. First, why is the thermal mode solution highly asymmetric, and how sensitive is the thermohaline circulation to the land-sea distribution of Late Permian? Second, is a hydrologic cycle double the intensity of today's a plausible scenario during the Late Permian? *Manabe and Stouffer* [1994] showed that in a CO_2 quadrupling experiment the intensity of the net freshwater flux $E - P$ increased to $\sim$ 1.5 of the present level. In the Late Permian the PCO_2 level could have been very much higher than that of today [*Budyko and Ronov*, 1979]. Moreover, increased dust and sulphate aerosols due to stronger volcanic activity during the Late Permian could also induce stronger freshwater flux [*Kozur*, 1998]. It is also notable that in a warm, equable climate the smaller the polar-equator surface temperature gradient is, the weaker the critical intensity of $E - P$ required to induce the haline mode is [*Zhang et al.*, manuscript in preparation, 2001].

It should be said that our results seem difficult to recon-

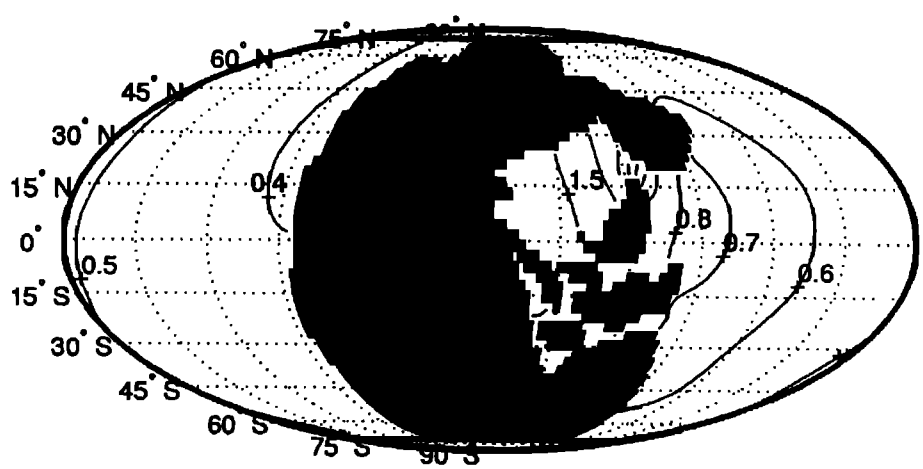

Figure 9. Possible oxygen distribution (mL/L) at bottom of the ocean with the Late Permian haline mode ocean circulation.

cile with a persistent (20 million year), ocean-wide, deepwater anoxic event across the Permo - Triassic (P/T) boundary [*Isozaki*, 1997]. However, most geological records for the Late Permian do not resolve the timescales (a few thousand years) of the thermohaline oscillations discussed in this paper. It is possible that the properties of long periods of haline mode circulation could dominate the cycle and the time-averaged sediment samples, leading to the appearance of a sustained anoxia. The sulfur isotope record [*Kajiwara et al.*, 1994] suggests that the extended period of anoxia is punctuated by a temporary, massive mixing across the P/T boundary. The deep ocean is interpreted to have been oxic during this mixing episode despite the presence of black shales in the sediments [Kajiwara et al., 1994]. This study suggests that such evidence could be consistent with long-term (many thousands of years) changes between haline and thermal mode ocean states. On these longer timescales, such changes might be forced by variations in external forcing and the inherent instability of the haline mode.

In summary, while these model results are not easily reconciled with the notion of truly persistent, deep-ocean anoxia induced by changes in ocean circulation, they illustrate possible mechanisms of ocean circulation and biogeochemistry which may be consistent with the sedimentary record.

Acknowledgments. We thank D. B. Rowley for providing us with his topographic reconstructions of the Late Permian. Discussions with John Edmond, Ed Boyle, Jochem Marotzke, and Carl Wunsch were very helpful. The numerical calculations were carried out on Pleaides, a cluster of workstations donated by Compaq-Digital housed in MIT's Laboratory for Computer Science. This work was supported by NSF grant OCE-964331.

References

Berner, R. A., and D. E. Canfield, A new model for atmospheric oxygen over Phanerozoic time, *Am. J. Sci., 289*, 333-361, 1989.

Bryan, F., High-latitude salinity effects and interhemispheric thermohaline circulation, *Nature, 323*, 301-304, 1986.

Budyko, M. I., and A. B. Ronov, Atmospheric evolution in the Phanerozoic, *Geochem. Int., 16*, 1-9, 1979.

Erwin, D. H., The Permo-Triassic extinction, *Nature, 367*, 231-235, 1994.

Gent, P. R., and J. C. McWilliams, Isopycnal mixing in ocean circulation models, *J. Phys. Oceanogr., 20*, 150-155, 1990.

Haney, R. L., Surface thermal boundary condition for ocean circulation models, *J. Phys. Oceanogr., 1*, 241-248, 1971.

Hotinski, R. M., K. L. Bice, L. R. Kump, R. G. Najjar, and M. A. Arthur, Ocean stagnation and end-Permian anoxia. *Geology, 29*, 7-10, 2001.

Huang, R. X., Thermohaline circulation: Energetics and variability in a single-hemisphere basin model, *J. Geophys. Res., 99*, 12,471-12,485, 1994.

Ishiwatari, A., Time-space distribution and petrologic diversity of Japanese ophiolites, in *Ophiolite Genesis and Evolution of the Oceanic Lithosphere*, edited by T. Peters, A. Nicolas, and R. G. Coleman, pp. 723-743, Kluwer Acad., Norwell, Mass., 1991.

Isozaki, Y., Permo - Triassic boundary superanoxia and stratified superocean: records from lost deep sea, *Science, 276*, 235-238, 1997.

Kajiwara, Y., S. Yamakita, K. Ishida, H. Ishiga, and A. Imai, Development of a largely anoxic stratified ocean and its temporary massive mixing at the Permian/Triassic boundary supported by the sulfur isotopic record, *Palaeogeogr., Palaeoclimatol., Palaeoecol., 111*, 367-379, 1994.

Knoll, A. H., R. K. Bambach, D. E. Canfield, and J. P. Grotzinger, Comparative Earth history and Late Permian mass extinction, *Science, 273*, 452-457, 1996.

Kozur, H. W., Some aspects of the Permian-Triassic boundary (PTB) and of the possible causes for the biotic crisis around this boundary, *Palaeogeogr., Palaeoclimatol., Palaeoecol., 143*, 227-272, 1998.

Kutzbach, J. E., and R. G. Gallimore, Pangaean climates: Megamonsoons of the megacontinent, *J. Geophys. Res., 94*, 3341-3358, 1989.

Kutzbach, J. E., P. J. Guetter, and W. M. Washington, Simulated circulation of an idealized ocean for Pangaean time, *Paleoceanography, 5*, 299-317, 1990.

Ledwell, J. R., A. J. Watson, and C. S. Law, Evidence for slow mixing across the pycnocline from an open-ocean tracer-release experiment, *Nature, 364*, 701-703, 1993.

Levitus, S., and T. Boyer, *World Ocean Atlas 1994 Volume 2: Oxygen*, NOAA Atlas NESDIS 2, U.S. Department of Commerce, Washington, D.C., 1994.

Levitus, S., R. Burgett, and T. Boyer, *World Ocean Atlas 1994 Volume 3: Nutrients*, NOAA Atlas NESDIS 3, U.S. Department of Commerce, Washington, D.C., 1994.

Lohrenz, S. E., G. A. Knauer, V. L. Asper, M. Tuel, and A. H. Knap, Seanonal variability in primary production and particle flux in the northwestern Sargasso Sea: U.S. JGOFS Bermuda Atlantic Time-series Study, *Deep Sea Res., 39*, 1373-1391, 1992.

Manabe, S., and R. J. Stouffer, Two stable equilibria of a coupled ocean-atmosphere model, *J. Clim., 1*, 841-866, 1988.

Manabe, S., and R. J. Stouffer, Multiple-century response of a coupled ocean-atmosphere model to an increase of atmospheric carbon dioxide, *J. Clim , 7*, 5-23, 1994.

Marotzke, J., Instabilities and multiple steady states of the thermohaline circulation, in *Oceanic Circulation Models: Combining Data and Dynamics*, edited by D. L. T. Anderson and J. Willebrand, pp. 501-511, Kluwer Acad., Norwell, Mass., 1989.

Marotzke, J., Boundary mixing and the dynamics of three-dimensional thermohaline circulations, *J. Phys. Oceanogr., 27*, 1713-1728, 1997.

Marotzke, J., and J. Willebrand, Multiple equilibria of the global thermohaline circulation, *J. Phys. Oceanogr., 21*, 1372-1385, 1991.

Marshall, J., and F. Schott, Open ocean deep convection: Observations, models and theory, *Rev. Geophys., 37*, 1-64, 1999.

Marshall, J., C. Hill, L. Perelman, and A. Adcroft, Hydrostatic, quasi-hydrostatic, and nonhydrostatic ocean modeling, *J. Geophys. Res., 102*, 5733-5752, 1997a.

Marshall, J., A. Adcroft, C. Hill, L Perelman, and C. Heisey, A finite-volume, incompressible Navier Stokes model for studies of the ocean on parallel computers, *J. Geophys. Res., 102*, 5753-5766, 1997b.

Martin, J. H., G. A. Knauer, D. M Karl, and W. W. Broenkow, VERTEX: Carbon cycling in the northeast Pacific, *Deep Sea Res., 34*, 267-285, 1987.

Munk, M., and C. Wunsch, Abyssal recipes II: Energetics of tidal and wind mixing, *Deep Sea Res., Part I, 45*, 1977-2010, 1998.

Najjar, R. G., J. L. Sarmiento, and J. R. Toggweiler, Downward transport and fate of organic matter in the ocean: Simulations with a general circulation model, *Global Biogeochem. Cycles, 6*, 45-76, 1992.

North, G. R., R. F. Cahalan, and J. A. Coakley Jr., Energy balance climate models, *Rev. Geophys., 19*, 91-121, 1981.

Paltridge, G. W., and C. M. R. Platt, *Radiative Processes in Meterology and Climatology*, Elsevier Sci., New York, 1976.

Parsons, T. R., M. Takahashi, and B. Hargrave, *Biological Oceanographic Processes*, Pergamon, New York, 1988.

Railsback, L. B., S. C. Ackerly, T. F Anderson, and J. L. Cisne, Palaeontological and isotope evidence for warm saline deep waters in Ordovician oceans, *Nature, 343*, 156-159, 1990.

Saleeby, J. B., Petrotectonic and paleogeographic

settings of U.S. cordilleran ophiolites, in *The Cordilleran Orogen: Contemtinous U.S., The Geology of North America*, Vol. G-3, edited by B. C. Burchfiel, P. W. Lipman. and M. L. Zoback, pp. 653-682, Geol. Soc. of Am., Boulder, Colo., 1992.

Sarmiento, J. L., T. D. Herbert, and J. R. Toggweiler, Causes of anoxia in the world ocean, *Global Biogeochem. Cycles, 2*, 115-128, 1988.

Stommel, H., Thermohaline convection with two stable regimes of flow, *Tellus, 13*, 224-230, 1961.

Takahashi, T., W.S. Broecker, and S. Langer, Redfield ratio based on chemical data from isopycnal surfaces, *J. Geophys. Res., 90*, 6907-6924, 1985.

Taylor, E. L., T. N. Taylor, and N. R. Cuneo, The present is not the key to the past: A polar forest from the Permian of Antarctica, *Science, 257*, 1675-1677, 1992.

Toole, J. M., K. L. Polzin, and R. Schmitt, Estimates of diapycnal mixing in the abyssal ocean, *Science, 264*, 1120-1123, 1994.

Wanninkof, R., Relationship between wind speed and gas exchange over the ocean. *J. Geophys. Res., 97*, 7373-7382, 1992.

Weiss, R. F., The solubility of nitrogen, oxygen and argon in water and seawater, *Deep Sea Res., 17*, 721-735, 1970.

Wignall, P. B., and R. J. Twitchett, Oceanic anoxia and the end Permian mass extinction, *Science, 272*, 1155-1158, 1996.

Zhang, J. B., R. W. Schmitt, and R. X. Huang, The relative influence of diapycnal mixing and hydrologic forcing on the stability of the thermohaline circulation, *J. Phys. Oceanogr., 29*, 1096-1108, 1999.

Zhang, J. Z., and F. J. Millero, The chemistry of the anoxic waters in the Cariaco trench, *Deep Sea Res., 40*, 1023-1041, 1993.

M. J. Follows, J. P. Grotzinger, J. Marshall, and R. Zhang , Department of Earth, Atmospheric, and Planetary Sciences, MIT, Cambridge, MA 02139. (mick@plume.mit.edu; grotz@mit.edu; marshall@gulf.mit.edu; rong@gulf.mit.edu.)

(Received March 10, 2000;
revised December 27, 2000;
accepted January 26, 2001.)